Non-Linear Approximation of Reflectance Functions

Eric P. F. Lafortune Sing-Choong Foo * Kenneth E. Torrance Donald P. Greenberg

Program of Computer Graphics
Cornell University †

Abstract

We introduce a new class of primitive functions with non-linear parameters for representing light reflectance functions. The functions are reciprocal, energy-conserving and expressive. They can capture important phenomena such as off-specular reflection, increasing reflectance and retro-reflection. We demonstrate this by fitting sums of primitive functions to a physically-based model and to actual measurements. The resulting representation is simple, compact and uniform. It can be applied efficiently in analytical and Monte Carlo computations.

CR Categories: I.3.7 [Computer Graphics]: Three-Dimensional Graphics and Realism; I.3.3 [Computer Graphics]: Picture/Image Generation

Keywords: Reflectance function, BRDF representation

1 INTRODUCTION

The bidirectional reflectance distribution function (BRDF) of a material describes how light is scattered at its surface. It determines the appearance of objects in a scene, through direct illumination and global interreflection effects. Local reflectance *models* therefore play an essential role in local and global illumination simulations.

The diagram of Figure 1 illustrates the importance of a proper representation of reflectance data. The data originate from physical measurements, from scattering simulations on surfaces, from physically-based reflectance models, or from a set of empirical parameters input by the user. The representation should capture the necessary information in a way that allows it to be used in global illumination algorithms. Several factors contribute to the quality and usefulness of a representation: *accuracy*, *physical correctness* and *computational efficiency*.

First of all, the original data should be represented accurately enough to obtain physically faithful results. However, in practice, precise measurements are often not available. As a very precise representation cannot improve imprecise data, a simpler model that naturally interpolates the data may be preferable. It can also be useful to have a model with a limited set of parameters that are intuitive to use. Such parameters provide an easy way to control or to monitor the behavior of the model.

Secondly, the representation should be physically plausible. Reflectance functions are positive, reciprocal and energy-conserving [12]. Preferably, their representations should satisfy these constraints as well, because global illumination algorithms may rely on it.

Thirdly, for actual application in global illumination computations, the ideal model should be computationally efficient. It is usually an element in the larger context of an illumination simulation algorithm. One thus looks for a proper balance between accuracy, memory use and computation times of the various components. In the context of physically-based rendering, it makes little sense to use an overly precise and computationally expensive or memory-hungry model, when small subtleties are overwhelmed by global illumination effects, or when the simulation is relatively inaccurate.

At present, many reflectance models are not physically plausible. More precise physical models are often computationally expensive and geared toward specific types of surfaces. The most expressive models, such as spherical harmonics or wavelet representations, may require significant memory to obtain acceptable representations of even the simplest BRDFs. Yet we want to efficiently represent the relatively complex reflectance of common surfaces such as the wooden table shown in Figure 2. The pictures illustrate the varying specular and diffuse reflectance for different viewing angles.

In this paper we introduce a representation based on a new class of functions with non-linear parameters. While the representation does not offer the arbitrary accuracy that linear basis functions can achieve, it is expressive enough to fit complex reflectance behavior. Importantly, a single function can capture a complete BRDF over its entire domain of incident and exitant directions. It is therefore uniform and compact, as well as computationally efficient.

The next section gives a brief overview of previous work. Section 3 discusses the concept of non-linear approximation. We then present our specific primitive functions for modeling reflectance in Section 4. The qualitative properties of functions are discussed in Section 5, while quantitative fits to complex reflectance functions are presented in Section 6. Section 7 shows more results.

2 PREVIOUS WORK

Previous research focuses on various aspects of reflectance functions: their derivation, their measurement, and their representation. Torrance and Sparrow [22], and Cook and Torrance [3, 4] derived physical models based on geometrical optics, assuming specular V-grooves, and incorporating masking and self-shadowing effects. Their models correctly predict the off-specular reflection that they had previously measured [21]. Extending this work, He *et al.* [9] derived a model based on physical optics. The final representation of the model consists of an ideal diffuse component, a directional-diffuse component and a specular mirror component, which are all expressed by a set of analytic expressions. These can be evaluated numerically, albeit at a fair computational expense. Poulin

*Currently at Blue Sky Studios, Harrison, NY.
†580 Rhodes Hall, Ithaca, NY 14853, USA.
WWW: http://www.graphics.cornell.edu/
E-mail: eric@graphics.cornell.edu

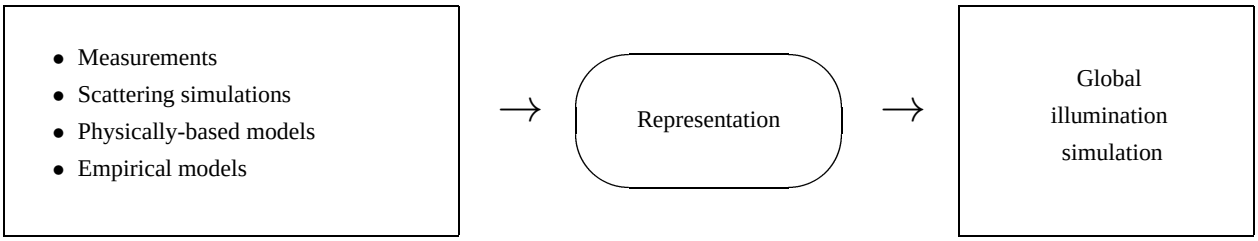

Figure 1: The representation of reflectance data constitutes the essential link between the origin of the raw data and their application in global illumination algorithms.

Figure 2: These pictures show a table exhibiting typical increasing specular reflection for increasingly grazing angles. At the same time the diffuse component, which results from subsurface scattering, fades out; the wood-grain texture and color disappear.

and Fournier [16] constructed a model assuming a surface consisting of microscopic cylinders. Oren and Nayar [14] derived a non-Lambertian diffuse model on the basis of diffuse micro-facets.

An alternative approach for deriving theoretical models is to perform a deterministic or Monte Carlo simulation on a surface model at a micro-scale. Kajiya [10] computed anisotropic reflectance functions based on the Kirchoff laws. He proposed storing the results in a table from which the values are linearly interpolated. Cabral [2] also stored reflectance simulation results in a table, but then represented them using spherical harmonics for a rendering step. Westin *et al.* [24] directly estimated the coefficients of the spherical harmonics. Hanrahan and Krueger [8] simulated subsurface scattering and stored the results in a uniform subdivision of the hemisphere. Gondek *et al.* [7] stored results in an adaptive subdivision of the geodesic sphere.

Empirical models, on the other hand, are not constructed from physical first principles. Instead, they capture reflectance effects using basis functions or other generic functions. The functions usually do not have any inherent physical meaning. Their physical validity stems from the theoretical or measured data to which they are fitted. For this purpose the functions should be expressive, while still being compact and efficient to use. Lambert's approximation, which assumes that the reflectance function of a diffuse surface is simply a constant, is widespread and sufficiently accurate for many applications. Phong [15] introduced one of the first more general shading models into computer graphics. Although it was not presented in the context of physically-based rendering, Lewis [12] showed how a physically plausible reflectance function can be derived from it. Ward [23] presented a model based on a Gaussian lobe, stressing its physical plausibility and ease of use. He successfully fitted the model to measurements of various surfaces and presented an equation to sample directions for it, which is important for Monte Carlo applications such as stochastic ray tracing. Schlick [17, 18] presented a model in which the important factors of previous physically-based models are approximated numerically, making it more convenient for use in Monte Carlo algorithms. Fournier [6] experimented with sums of separable functions for representing reflectance models, for application in radiosity algorithms. Schröder and Sweldens [19] represented reflectance functions using spherical wavelets. Koenderink *et al.* [11] recently introduced a compact representation based on Zernike polynomials.

Our work falls within the latter category of representations. We take a novel approach, using non-linear approximation with a sum of one or more appropriate functions. In the next section, we explain the general principle of non-linear approximation.

3 NON-LINEAR APPROXIMATION

Approximating functions with linear basis functions is well studied. Some common basis functions are Fourier bases, Chebychev polynomials and piece-wise linear functions. When approximating a function, the coefficients of the basis functions are determined by a set of linear equations. Non-linear approximation, for instance with rational functions or with Gaussians, is somewhat less known. In this approach, the parameters of the approximating functions are not necessarily linear with respect to the original function. They therefore generally have to be determined using non-linear optimization. Figure 3 shows an example of a peaked one-dimensional function that is approximated using the first four terms of a Fourier series and using two Gaussian functions. The Fourier terms vary in amplitude and in phase. Due to the relatively sharp peaks in the original function, their sum is only a rough approximation, which becomes negative at some point. The Gaussians are parametrized by a position, a standard deviation and a size. Their sum approximates the original function much better and remains positive over the interval. Obviously, this is not true in general, for all possible functions. However, the non-linear functions can be chosen such that they span a region of the function space that suits a specific application. Functions can then be approximated using a more compact representation. Furthermore, the parameters can be more intuitive when interpreting or controlling the model.

In the context of modeling BRDFs, more general representations are usually linear, e.g. spherical harmonics [2, 24], sums of separable bicubic polynomials [6] or wavelets [19]. Especially the former representations may require many coefficients, for instance

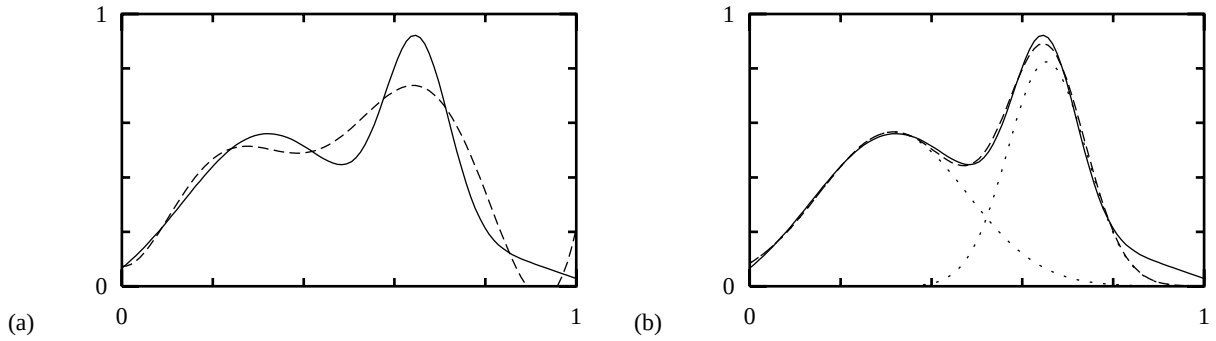

Figure 3: (a) A one-dimensional function (solid line) and its approximation by the first four terms of the Fourier series (dashed line). (b) The same function (solid line) and its approximation by the sum of two unconstrained Gaussians (dashed line). The Gaussians (dotted lines) correspond directly to the main features of the function.

for specular surfaces, which have reflectance functions with high frequencies. On the other hand, many popular models are simple non-linear approximations. The cosine lobe model [12] and the Gaussian model by Ward [23] are probably the most widely used examples, being simple and efficient. Instead of fitting a function in one dimension as in Figure 3, these approximations are defined in the four directional dimensions of the reflectance function.

In this work we take the idea of non-linear approximation a step further, paying close attention to physical plausibility and ensuring computational efficiency.

4 THE GENERALIZED COSINE MODEL

Our representation is a generalization of the cosine lobe model that is based on the Phong shading model. As such, it is intended to approximate the directional-diffuse component and possibly a non-Lambertian diffuse component of a reflectance function. We first discuss the cosine lobe model and then our generalization.

4.1 The Classical Cosine Lobe Model

The original cosine lobe model is attractively simple, but it has a few major shortcomings for representing directional-diffuse reflection. Figure 5 shows the appearance of the model for different viewing angles. The behavior contrasts sharply with the reflectance behavior of most real surfaces, which appear more specular at grazing angles, because the apparent roughness decreases (Figure 2). So why do the reflections in the images of Figure 5 disappear? There are two related reasons. Figure 4a shows how the shape and size of the reflectance lobe remain the same for all incident directions. For grazing angles, up to half the lobe disappears under the surface. Furthermore, the remaining part has to be multiplied by the cosine of the angle with the normal when computing the reflected power. As illustrated in Figure 4b, this results in the albedo (the directional-hemispherical reflectance) decreasing rapidly towards grazing angles. Visually, this means that the directional-diffuse reflection will disappear rather than increase.

In spite of these flaws, the original cosine lobe model is still widely used for illumination simulations. The model is physically plausible: it is reciprocal and conservation of energy can be ensured easily. It is simple and computationally inexpensive to evaluate. It is attractive for Monte Carlo algorithms as one can easily sample directions according to the function. In the context of deterministic algorithms, Arvo [1] showed how irradiance tensors can be applied to analytically compute cosine lobe reflections on surfaces illuminated by diffuse luminaires.

We briefly recall that the original cosine lobe model for a given position and wavelength can be written formally as follows:

$$f_r(\mathbf{u},\mathbf{v}) \quad = \quad \rho_s C_s \cos^n \alpha, \tag{1}$$

where α is the angle between the exitant direction $\mathbf{v}$ and the mirror direction of the incident direction $\mathbf{u}$, which we will denote by $\mathbf{u}_m$. In order not to burden our notation we will define the power of negative values as 0; the lobe is clamped to 0 for negative cosine values. If we choose C_s to be the normalization factor $(n+2)/(2\pi)$, then ρ_s is a value between 0 and 1, expressing the maximum albedo of the lobe. This maximum is reached for perpendicularly incoming light. The maximum albedo ρ_s and the specular exponent n are the parameters that determine the size and shape of the reflectance function. The cosine can be written as a dot product, and as mentioned in [1], the mirroring around the normal $\mathbf{n}$ can be written using a Householder matrix:

$$\begin{aligned} f_r(\mathbf{u},\mathbf{v}) &= \rho_s C_s \left[\mathbf{u}_m \cdot \mathbf{v}\right]^n \\ &= \rho_s C_s \left[\mathbf{u}^T (2\mathbf{n}\mathbf{n}^T - \mathbf{I})\mathbf{v}\right]^n. \end{aligned} \tag{2}$$

4.2 The Generalized Cosine Lobe Model

Our model can be regarded as a generalization of the original cosine lobe model. Most known generalizations simply scale the reflectance lobes in some way, violating reciprocity in the process. Changing the model while still satisfying the reciprocity constraint is hard. Physical plausibility, and reciprocity in particular, are therefore important merits of the generalization presented. Yet the representation is conceptually simple and it retains the original advantages for Monte Carlo sampling and analytical evaluation. As a result, it can easily be integrated into existing code.

The essential observation is that Equation 2 can be generalized by replacing the Householder transform together with the normalization factor by a general 3×3 matrix $\mathbf{M}$:

$$f_r(\mathbf{u},\mathbf{v}) \quad = \quad \rho_s \left[\mathbf{u}^T \mathbf{M} \mathbf{v}\right]^n, \tag{3}$$

where we assume that the direction vectors are defined with respect to a fixed local coordinate system at the surface. This representation provides us with 9 coefficients and an exponent to shape the reflectance function. Of course, certain physical restrictions apply to these parameters. In order for this reflectance function to be reciprocal, the matrix has to be symmetrical: $\mathbf{M} = \mathbf{M}^T$.

We can now apply a singular value decomposition of $\mathbf{M}$ into $\mathbf{Q}^T\mathbf{D}\mathbf{Q}$. This yields the transformation $\mathbf{Q}$ for going to a new local coordinate system, in which the matrix simplifies to the diagonal matrix $\mathbf{D}$. Except for unusual types of anisotropy, the axes

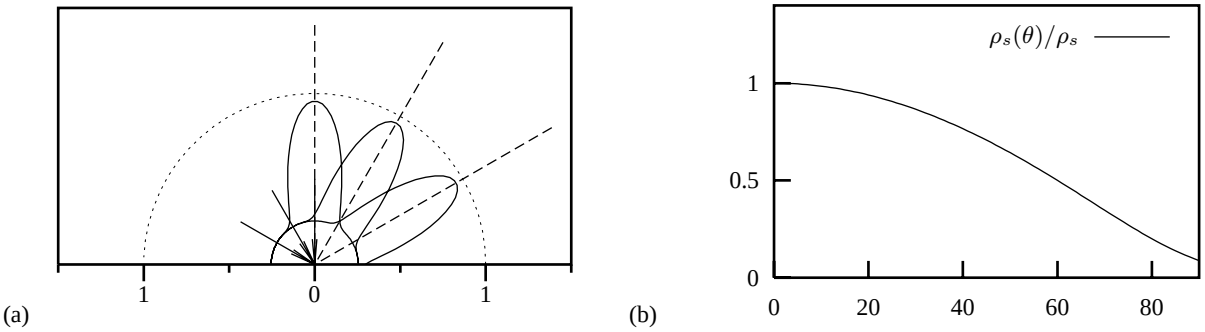

Figure 4: (a) Polar plots of the classical cosine lobe reflectance model ($\rho_s = 0.2$, $n = 20$) with a Lambertian term ($\rho_d = 0.8$) in the incidence plane, for incidence angles $0°$, $30°$ and $60°$. (b) The relative decrease of the albedo of the directional-diffuse term as a function of incidence angle.

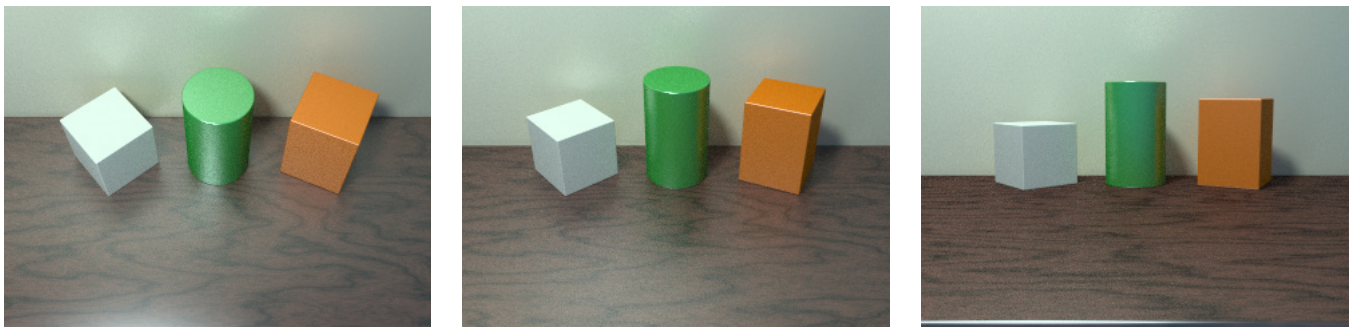

Figure 5: Rendered pictures of a scene with the classical cosine lobe model, for various viewing angles. The glossy reflection on the table disappears at grazing angles, which is exactly the opposite of real surface behavior.

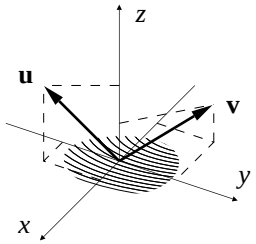

Figure 6: The incident direction **u** and exitant direction **v** are defined in a local coordinate system at the surface. The coordinate system is aligned to the normal and to the principal directions of anisotropy, if any.

are now aligned to the normal and to the principal directions of anisotropy, as illustrated in Figure 6. The diagonal matrix can be seen as weighting the terms of the dot product $\mathbf{u} \cdot \mathbf{v}$:

$$f_r(\mathbf{u},\mathbf{v}) \quad = \quad \rho_s \left[C_x u_x v_x + C_y u_y v_y + C_z u_z v_z\right]^n. \qquad (4)$$

This formulation of the model is the most convenient to use. In the case of isotropic reflection, $C_x = C_y$. The original cosine lobe model is obtained by choosing $-C_x = -C_y = C_z = \sqrt[n]{C_s}$. However, much more expressive functions than the cosine lobe model can be obtained by varying the different parameters, as we will show in more detail in Section 5. Note that the function is defined for all incident and exitant directions. It is thus fully four-dimensional and we apply and fit it as such.

4.3 The Generalized Function as a Cosine Lobe

The generalized function has an elegant and very practical property: for each given incident direction **u** the function can be rewritten as a scaled version of an ordinary cosine lobe. Simply rewriting Equation 3:

$$\begin{aligned} f_r(\mathbf{u},\mathbf{v}) \quad &= \quad \rho_s \left\|\mathbf{u}^T\mathbf{M}\right\|^n \left[\frac{\mathbf{u}^T\mathbf{M}}{\left\|\mathbf{u}^T\mathbf{M}\right\|}\mathbf{v}\right]^n \\ &= \quad \rho_s C_s(\mathbf{u}) \left[\mathbf{u}' \cdot \mathbf{v}\right]^n \\ &= \quad \rho_s C_s(\mathbf{u}) \cos^n \alpha'. \end{aligned} \qquad (5)$$

The direction $\mathbf{u}' = (\mathbf{u}^T\mathbf{M}/\|\mathbf{u}^T\mathbf{M}\|)^T$ is a transformed and normalized version of the incident direction **u**, and the angle α' is its angle with **v**. The scaling factor $C_s(\mathbf{u}) = \|\mathbf{u}^T\mathbf{M}\|^n$ is a power of the normalization factor and therefore varies with the incident direction. For the specific case of Equation 4, the direction $\mathbf{u}' = (C_x u_x, C_y u_y, C_z u_z)^T / \sqrt{C_x^2 u_x^2 + C_y^2 u_y^2 + C_z^2 u_z^2}$ and the scaling factor $C_s(\mathbf{u}) = \sqrt{C_x^2 u_x^2 + C_y^2 u_y^2 + C_z^2 u_z^2}^n$. This observation shows how the original cosine lobe function is now generalized in its orientation and its scaling. The changes in orientation and scale are specific results of Equation 3 – if they were just arbitrary, reciprocity would generally not be preserved.

Practically, the equation makes it straightforward to continue using the same Monte Carlo sampling strategies and deterministic evaluation techniques as for the original cosine lobe model. One only needs to substitute the mirror direction $\mathbf{u}_m$ by $\mathbf{u}'$ (or the angle α by α') and scale the results as required. For instance, the albedo $\rho_s(\mathbf{u})$ for each incident direction **u** can be computed analytically, using the procedures presented by Arvo [1]. This is specifically useful to ensure energy conservation.

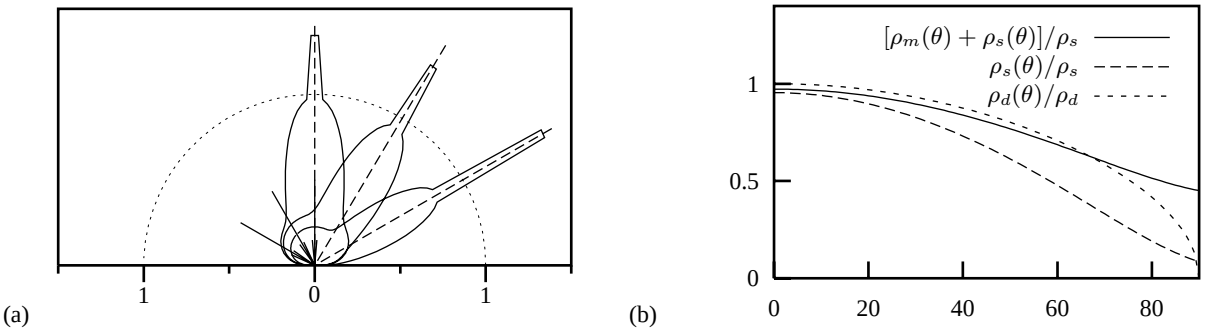

Figure 7: (a) Polar plots of the classical cosine lobe model ($\rho_s = 0.2$, $n = 20$) with a generalized diffuse term ($\rho_d = 0.8$, $n = 0.5$) and an additional mirror term ($R_m = 0.4$). (b) The albedos of the diffuse and directional-diffuse terms, $\rho_d(\theta)$ and $\rho_s(\theta)$ respectively, decrease towards grazing angles; the mirror term $\rho_m(\theta)$ gradually takes over.

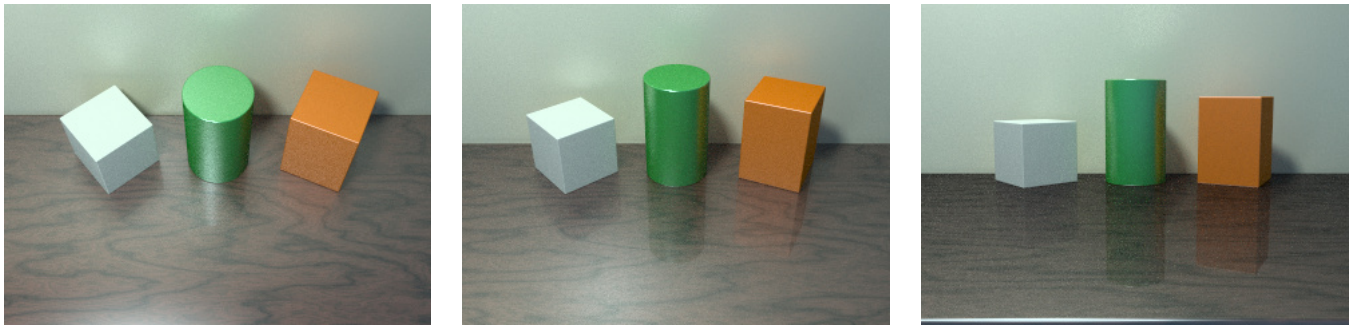

Figure 8: Rendered pictures of a scene with the classical cosine lobe model, now including the mirror term and a generalized diffuse term. The mirror term gradually takes over from the directional-diffuse term, and the diffuse term fades out. Even with these minor changes the table surface already shows a more realistic reflective behavior.

5 QUALITATIVE PROPERTIES

In this section, we illustrate the qualitative properties of our generalized model. We construct a few simple reflectance functions with diffuse, directional-diffuse and specular components, to demonstrate how the model can simulate important aspects of real-life reflectance behavior. Section 6 will then demonstrate the quantitative properties of the model, by fitting sums of primitive functions to a complex physically-based model and to actual measurements.

5.1 Non-Lambertian Diffuse Reflection

An effect apparent in the pictures of Figure 2 is the fading out of the diffuse component for grazing angles. As more light is reflected off the coating of the surface, the subsurface scattering responsible for the diffuse reflection diminishes. The surface looks less saturated and the wood texture disappears. While our generalized cosine lobe model encompasses the Lambertian model (by setting $n = 0$), a more general *rotationally symmetric* diffuse component can be derived from Equation 4, by setting $C_x = C_y = 0$:

$$f_r(\mathbf{u}, \mathbf{v}) \quad = \quad \rho_d C_d \, [u_z v_z]^n, \tag{6}$$

where the normalization factor $C_d = (n + 2)/(2\pi)$, and ρ_d is the parameter between 0 and 1 specifying the maximum albedo. For grazing incident or exitant directions the reflectance decreases proportionally to a power of the cosine of the angle with the normal. This instance actually corresponds to the model presented by Minnaert [13], in the context of modeling the reflectance of the lunar surface. The non-Lambertian diffuse component is plotted in Figure 7a (appearing as the small circular component near the origin), along with directional-diffuse and mirror components that will be discussed in the next section. Figure 7b shows the behavior of the albedo $\rho_d(\mathbf{u})$ as a function of incidence angle θ, normalized by the parameter ρ_d. Figure 8 illustrates the effect visually: the diffuse component of the table surface fades out for grazing angles.

5.2 Specularity at Grazing Angles

The other important visual effect shown in the pictures of Figure 2 is the increasing specularity of the polished table surface at grazing angles. This behavior can be accounted for by extending the model of a diffuse lobe and a directional-diffuse lobe with a specular mirror term. The directional-diffuse lobe can in the simplest case be an ordinary cosine lobe. The mirror term can be made to reflect a fraction of the power that is not reflected by the directional-diffuse lobe. A simple instance of these two components thus becomes:

$$\begin{aligned} f_r(\mathbf{u}, \mathbf{v}) \quad = \quad & \rho_s C_s \, [\mathbf{u}_m \cdot \mathbf{v}]^n \\ & + (\rho_s - \rho_s(\mathbf{u})) \, R_m \, \delta(\mathbf{u}_m - \mathbf{v}), \end{aligned} \tag{7}$$

where $\delta(\mathbf{u}_m - \mathbf{v})$ is the Dirac delta function with respect to the canonical measure on the sphere. In this case it is convenient to choose $C_s = (n + 1)/(2\pi)$. The factor $\rho_s - \rho_s(\mathbf{u})$ is the difference between the directional-diffuse scaling factor and the actual albedo for direction $\mathbf{u}$. The parameter R_m expresses the fraction of the power lost in the directional-diffuse lobe that is reflected in the mirror term. In Monte Carlo simulations this can be taken quite literally. One can sample a direction according to the cosine lobe. Any sample is then tested against the cosine of the angle with the normal, with rejection sampling. The fraction R_m of rejected samples is sent into the mirror direction. In analytical computations each of the terms, including the mirror term, can be computed.

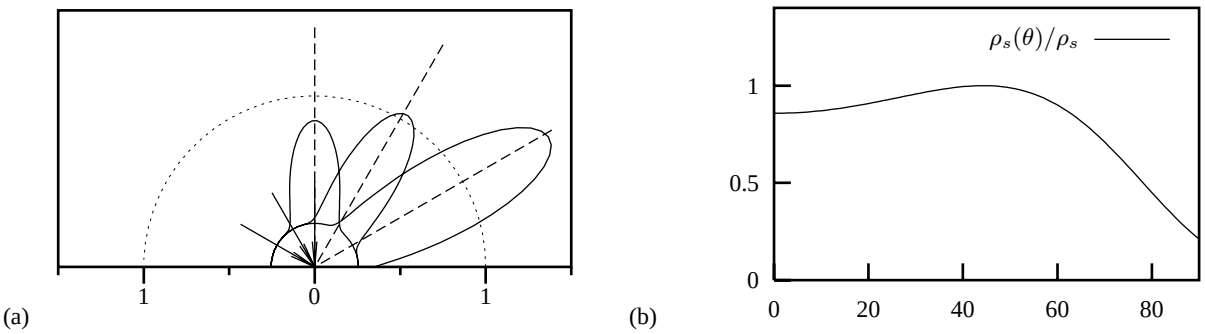

Figure 9: (a) Polar plots of the generalized cosine lobe model ($\rho_s = 0.2$, $n = 20$, $C_z/C_x = 0.95$) with a Lambertian term ($\rho_d = 0.8$). The lobes are slightly off-specular and increase in size towards grazing angles. (b) The albedo of the directional-diffuse term only decreases for larger incidence angles as a result.

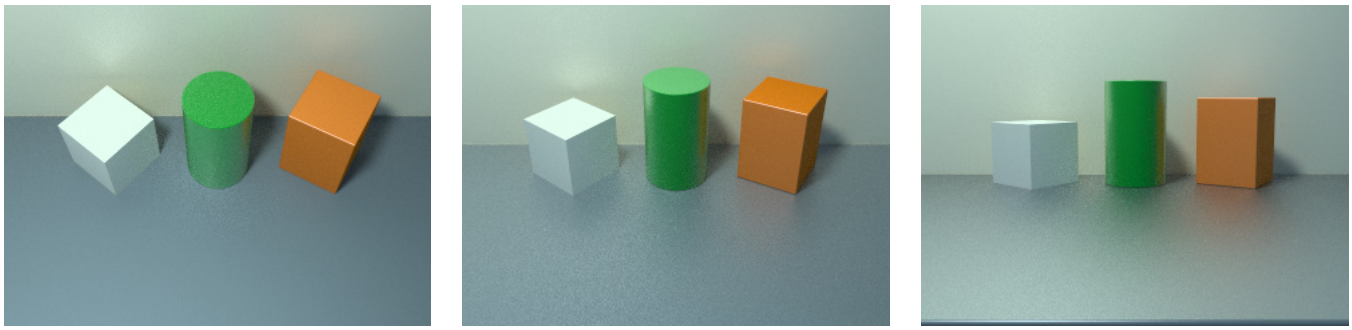

Figure 10: Rendered pictures of a scene with the generalized cosine lobe model. The off-specular directional-diffuse reflectance of the table surface gradually increases for grazing angles.

Figure 7 presents an example function, including the non-Lambertian diffuse reflection that was discussed in the previous section. Note that the mirror term is actually a Dirac delta function; it is broadened here to visualize its behavior. Figure 7b displays the albedos $\rho_s(\theta)$ and $\rho_m(\theta)$ for the directional diffuse and the mirror terms, respectively. Figure 8 then shows the example scene rendered with the extended model.

The results look reasonably realistic because the mirror term is a rough approximation of an actual Fresnel term multiplied by masking-shadowing and roughness factors (e.g. [9]). If it is known, a more accurate approximation can be used by attenuating the mirror term, so that R_m becomes a function of incidence angle.

5.3 Off-Specular Reflection

Application of the model becomes more interesting by varying the individual parameters of Equation 4. Torrance and Sparrow [21] already observed that the directional-diffuse lobe for a given incident direction generally does not reach its maximum for the mirror direction, but rather for a more grazing direction. At the same time the size of the reflectance lobe increases. The original cosine lobe model obviously does not account for these effects. This shortcoming is sometimes overcome by dividing by the cosine of the exitance angle, which breaks reciprocity. In the generalized model, parameters C_z that are smaller than $-C_x = -C_y$ yield a range of off-specular reflection effects, without compromising the physical plausibility. Figure 9 gives an example with moderately increasing reflectance, and Figure 10 shows a set of rendered images. The table surface exhibits off-specular reflection. It looks mostly diffuse from above, while the directional-diffuse component increases for grazing angles.

5.4 Retro-Reflection

Many surfaces not only scatter light in the forward direction, but also backwards, in the direction of the illuminant. This phenomenon is called retro-reflection. The moon surface is an extreme example, where a large fraction of light from the sun is reflected in the incident direction. In the generalized model, a retro-reflective lobe can be represented in the same uniform framework by using a set of parameters C_x, C_y and C_z that are all positive. The reflectance measurements of paint in section 6.2 will illustrate this effect.

5.5 Anisotropy

Anisotropic reflection can be modeled with a single primitive function, by assigning different values to the parameters C_x and C_y. As with the parameter C_z that controls the off-specular reflection, this will pull the reflectance lobes for all incident directions in a preferential direction and scale them. More general anisotropy, e.g. with a splitting lobe, can be obtained by constructing a matrix $\mathbf{M}$ for Equation 3 that is not necessarily symmetrical. Adding a reflectance term with its transpose $\mathbf{M}^T$ then yields a new reciprocal model.

6 QUANTITATIVE PROPERTIES

In this section, we show how the model is also suitable for representing complex real-life reflectance functions. The representation is a sum of several primitive functions of the form of Equation 4. Absorbing the albedo ρ_s in the other parameters, each primitive function i is defined by the parameters $C_{x,i} (= C_{y,i})$, $C_{z,i}$ and n_i.

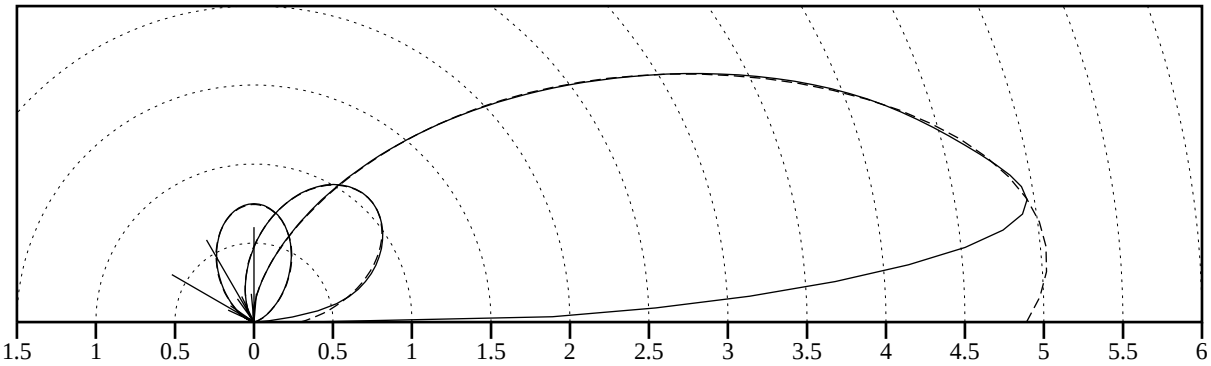

Figure 11: Polar plots of the fitted reflectance model (dashed lines) against the original physically-based model of a roughened aluminum surface (solid lines) in the plane of incidence, for $\theta = 0^\circ, 30^\circ, 60^\circ$, at $500nm$. The reflectance function becomes more off-specular and strongly increases in size towards grazing angles. The sum of generalized cosine functions captures these effects.

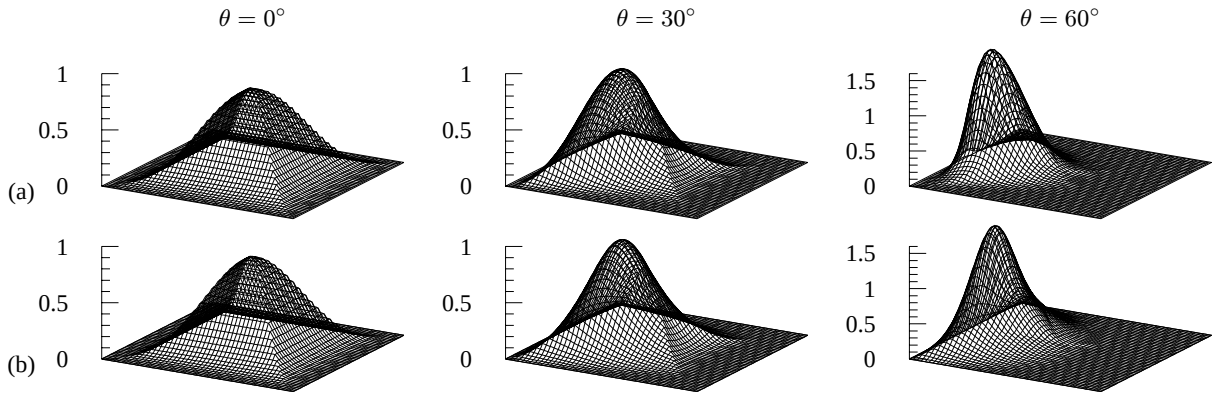

Figure 12: Plots of the original physically-based model of roughened aluminum (top row, a) and of the fitted reflectance model (bottom row, b), now multiplied by the cosines of the incidence and exitance angles with the normals, fitted and shown over the entire hemisphere, for various incidence angles.

The model can thus be written as:

$$f_r(\mathbf{u},\mathbf{v}) \quad = \quad \sum_i [C_{x,i}u_x v_x + C_{y,i}u_y v_y + C_{z,i}u_z v_z]^{n_i}. \quad (8)$$

The model is fitted to the BRDF of aluminum, based on the physically-based reflectance model of He *et al.*, and to the measured BRDF of blue paint. We minimize the mean-square error of the reflectance functions multiplied by the cosines of the incidence and exitance angles with the normal. As the primitive functions are non-linear, a non-linear optimization technique is required to determine the parameters. The Levenberg-Marquardt optimization algorithm has proven to be efficient for this application; computing each approximation requires only a few minutes in a standard numerical package. This is not a serious penalty, as it only has to be done once for each measured material.

In both case studies, we first look at the BRDFs in the incidence plane, and then in the entire function space. In the incidence plane the function space is two-dimensional, depending on the incident polar angle and the exitant polar angle. The entire function space of isotropic BRDFs is three-dimensional, additionally depending on the exitant azimuthal angle.

6.1 Fit to a Physically-Based Model

The reflectance model derived by He *et al.* [9] is generally acknowledged as the most sophisticated model in use in computer graphics. It consists of a Lambertian term, a directional-diffuse term and a mirror term. Here we concentrate on approximating the directional-diffuse term. In our example, the Lambertian term and the mirror term are mostly negligible, but in any case representing and using these terms is straightforward. We present the results for roughened aluminum, as in their original paper for wavelength $\lambda = 500nm$, roughness $\sigma_0 = 0.28\mu m$ and autocorrelation length $\tau = 1.77\mu m$.

Figure 11 shows the results of a fit in the incidence plane, using the sum of three primitive functions. It is important to note that the function has not been fitted for each of the individual lobes, which would be a lot easier, but to the reflectance function as a whole. The fit is visually perfect, except for more grazing angles. In this regime of angles, most of the difference is due to the masking term, which is not present in the representation. These values are less important, however, as they are multiplied in illumination computations by the cosine of the angle between the direction and the surface normal. Additionally, the mirror reflection becomes more important than the directional-diffuse reflection for grazing angles.

Figure 12 shows the results of fitting the approximation to the reflectance function in the entire three-dimensional space of directions. The functions are plotted for three different incidence angles, in a uniform parametrization of the hemisphere [20]. The creases along the diagonals of the square are a result of the parametrization and are not related to the functions. The functions are multiplied by the cosine of the exitance angle with the normal, so that the volumes below the surfaces are proportional to the albedos. Both the shapes of the functions and the albedos match very well.

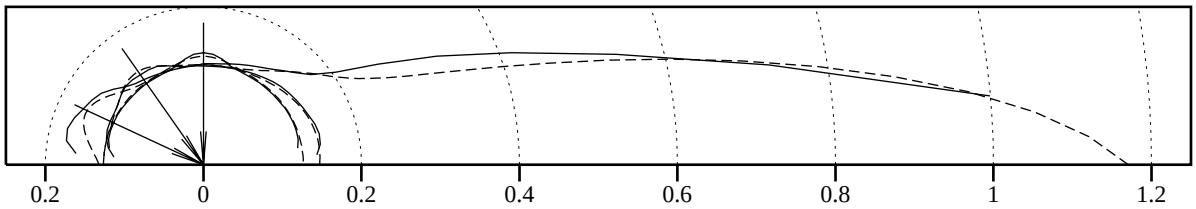

Figure 13: Polar plots of the fitted reflectance model (dashed lines) against the original measured BRDF data of blue paint (solid lines) in the plane of incidence, for $\theta = 0^\circ, 35^\circ, 65^\circ$, at $550nm$. The model successfully reproduces both the increasing retro-reflection and off-specular reflection.

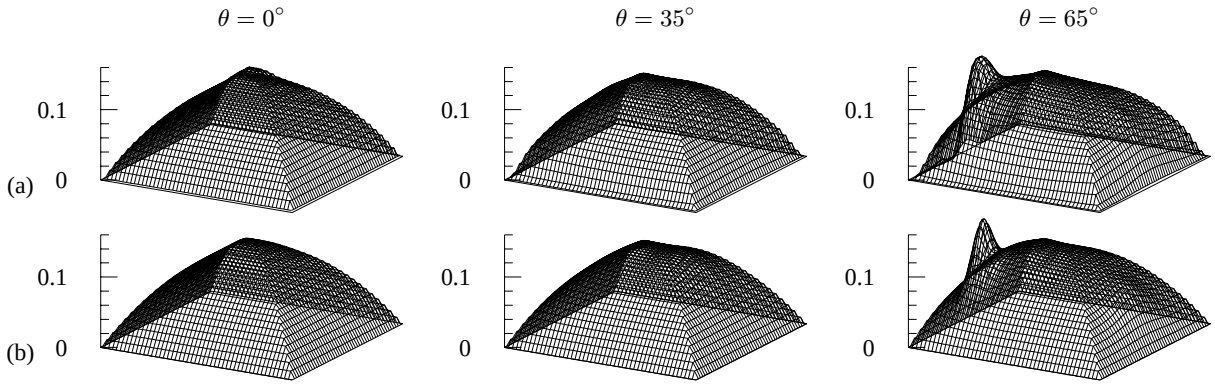

Figure 14: Plots of the original measured model of blue paint (top row, a) and of the fitted reflectance model (bottom row, b), now fitted and shown over the entire hemisphere, for various incidence angles.

6.2 Fit to Reflectance Measurements

The second comparison is with the measured reflectance data of a blue paint sample (spray-painted latex blue paint, Pratt & Lambert, Vapex Interior Wall Base 1, Color #1243, Cal. III) [5]. Figure 13 shows the data and the approximation in the incidence plane at $550nm$, for three incidence angles.

Compared to the strong forward-scattering behavior of the roughened aluminum, the paint is largely diffuse. Due to measurement noise, the data are more irregular. Still, there are important other phenomena. The forward scattering lobe increases rapidly for grazing angles and is very off-specular. The measurements did not include highly grazing angles, for which theory predicts a drop-off. The measurements did show increasing retro-reflection. The approximation, which uses a sum of three directional-diffuse functions and a Lambertian term, captures this effect.

Figure 14 shows the data and the approximation fitted over the three-dimensional space of incident and exitant directions. Table 1 lists the coefficients for this approximation, illustrating how simple and compact the model is. The positive value of C_x for lobe I indicates that it is a retro-reflective lobe, while lobes II and III account for the forward scattering. The ratios of the parameters C_x and C_z give an idea of how off-specular the lobes are and how fast they increase in size for grazing angles. Note that the exponents are not necessarily integers. For Monte Carlo simulations using the model, this is generally not a problem. For analytical computations the exponents would have to be constrained to integer values.

Lobe	$C_x = C_y$	C_z	n
I	0.86	0.77	18.6
II	-0.41	0.018	2.58
III	-1.03	0.70	63.8
Diffuse	0.13		

Table 1: The coefficients of the representation for the three-dimensional fit of Figure 14.

7 RESULTS

We have approximated the measured reflectance data of the blue paint presented in Section 6.2 and of a standardized steel sample (Matte finished steel, Q-Panel Laboratory Products, Q-panel R-46) at 6 discrete wavelengths. The resulting models were then used for global illumination rendering, using a Monte Carlo path tracing program. The implementation required only a few additional lines of code. The reflectance functions are evaluated using Equation 8. For sampling an exitant direction for a given incident direction we construct a probability density function that is a linear combination of the primitive cosine reflectance lobes.

Figure 15 shows a rendering of a simple scene with two spheres, a Q-panel, and two colored light sources, positioned symmetrically with respect to the viewer. A larger white light source above the viewer illuminates the whole scene. The sphere on the left is rendered with a Lambertian diffuse approximation of the measured blue paint, while the sphere on the right is rendered with the generalized reflectance model. The latter sphere has both red and green highlights due to strong forward scattering. These are lacking on the Lambertian sphere. With a light source near the viewer, the right sphere has a slightly flatter appearance due to retro-reflection. The Q-panel has a completely different appearance, displaying a blurry metallic reflection of the colored lights and of the objects. The representation successfully captures these very different reflectance characteristics.

8 CONCLUSIONS

We have introduced an efficient representation for a wide range of bidirectional reflectance distribution functions. It is an interesting alternative for previous models of directional-diffuse reflectance, which required either simplified single-term representations, complex analytical expressions for specific classes of functions, or general but large representations with linear basis functions.

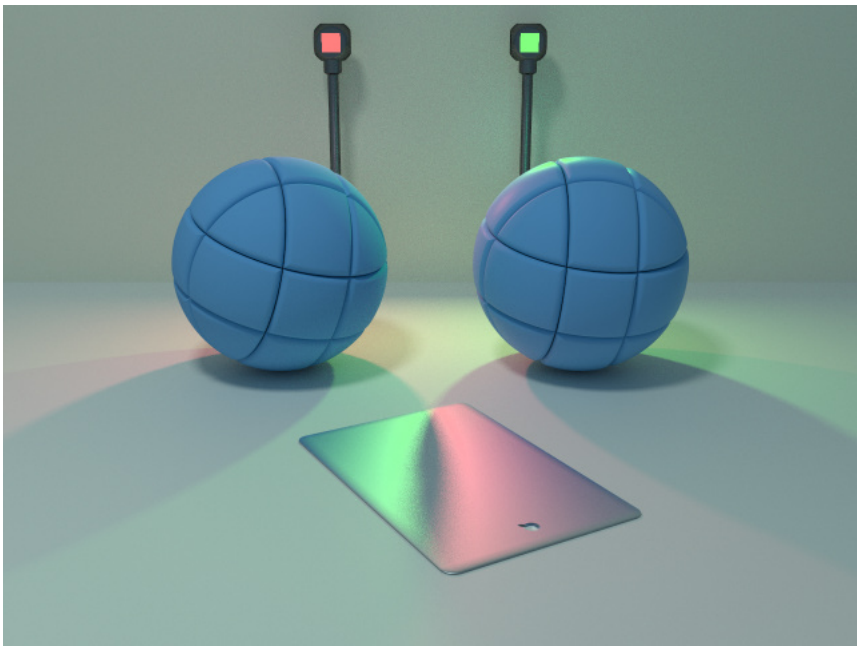

Figure 15: Rendered picture of a scene with two spheres and a Q-panel, illuminated by two colored light sources and one larger white light source. The sphere on the left has a Lambertian approximation of the measured paint reflectance; the sphere on the right is rendered with the non-linear approximation. The Q-panel has the non-linear approximation of the measured steel reflectance.

- The representation is compact. Each primitive function is determined by two or three coefficients and an exponent. Because the representation is memory-efficient, any complex wavelength dependency can be modeled by constructing independent approximations at discrete wavelengths.

- The functions are expressive. They can represent complex reflectance behavior, such as off-specular reflection, increasing directional-diffuse reflectance for grazing angles, retro-reflection and non-Lambertian diffuse reflection in a uniform way.

- The functions handle noise in the raw reflectance data gracefully. They can capture sharp reflectance lobes without suffering from small spurious errors in the data. If the data are sparse, the model interpolates them naturally.

- The functions themselves are physically plausible, irrespective of how they were constructed. They are inherently reciprocal. Energy-conservation can be verified analytically for each incident direction.

- On the algorithmic side, the representation is efficient and easy to use in both local and global illumination algorithms. Its simplicity and uniformity make it practical for implementation in hardware. In Monte Carlo algorithms, reflection directions for a given incident direction can be sampled according to the transformed cosine lobe. In deterministic algorithms, illumination from diffuse emitters can be computed analytically, using a straightforward extension of the calculations for ordinary cosine lobes.

- While the representation cannot approximate all possible reflectance functions to any desired accuracy, it adequately represents a range of measured BRDF data, which usually only have a very limited accuracy. In our tests, we have obtained satisfactory results with as few as three primitive functions to represent directional-diffuse reflections from roughened metals and paints. Broad, glossy reflectance lobes are relatively easy to approximate. Sharp directional-diffuse peaks, such as for smooth metal surfaces, may be harder to represent, due to a strong dependency on the Fresnel factor, which is not explicitly included in the representation.

As future work, we will look into the details of representing anisotropic reflectance measurements with one or more terms of the current model, e.g. to model the effect of splitting reflectance lobes at anisotropic surfaces.

Acknowledgements

Thanks to Pete Shirley for many helpful discussions on BRDF representations. Jon Blocksom provided the implementation of the He model. Also thanks to Ben Trumbore and Dan Kartch for critically reading the paper. Measurement equipment was provided by NSF CTS-9213183 and by the Imaging Science Division of the Eastman Kodak Company. Q-Panel Lab Products kindly provided the Q-panels. This work was supported by the NSF Science and Technology Center for Computer Graphics and Scientific Visualization (ASC-8920219) and by NSF ASC-9523483, and performed on workstations generously donated by the Hewlett-Packard Corporation.

References

[1] J. Arvo. Applications of irradiance tensors to the simulation of non-Lambertian phenomena. In *SIGGRAPH 95 Conference Proceedings*, pages 335–342, Los Angeles, California, August 1995.

[2] B. Cabral, N. Max, and R. Springmeyer. Bidirectional reflection functions from surface bump maps. *Computer Graphics*, 21(4):273–281, July 1987.

[3] R.L. Cook and K.E. Torrance. A reflectance model for computer graphics. *Computer Graphics*, 15(4):187–196, July 1981.

[4] R.L. Cook and K.E. Torrance. A reflectance model for computer graphics. *ACM Transactions on Graphics*, 1(1):7–24, January 1982.

[5] S.C. Foo. A gonioreflectometer for measuring the bidirectional reflectance of materials for use in illumination computations. Master's thesis, Cornell University, Ithaca, New York, July 1997.

[6] A. Fournier. Separating reflection functions for linear radiosity. In *Proceedings of the Sixth Eurographics Workshop on Rendering*, pages 383–392, Dublin, Ireland, June 1995.

[7] J.S. Gondek, G.W. Meyer, and J.G. Newman. Wavelength dependent reflectance functions. In *SIGGRAPH 94 Conference Proceedings*, pages 213–220, Orlando, Florida, July 1994.

[8] P. Hanrahan and W. Krueger. Reflection from layered surfaces due to subsurface scattering. In *SIGGRAPH 93 Conference Proceedings*, pages 165–174, Anaheim, California, August 1993.

[9] X.D. He, K.E. Torrance, F.X. Sillion, and D.P. Greenberg. A comprehensive physical model for light reflection. *Computer Graphics*, 25(4):175–186, July 1991.

[10] J. Kajiya. Anisotropic reflectance models. *Computer Graphics*, 19(4):15–21, July 1985.

[11] J.J. Koenderink, A.J. van Doorn, and M. Stavridi. Bidirectional reflection distribution function expressed in terms of surface scattering modes. In *European Conference on Computer Vision*, pages 28–39, 1996.

[12] R.R. Lewis. Making shaders more physically plausible. In *Proceedings of the Fourth Eurographics Workshop on Rendering*, pages 47–62, Paris, France, June 1993.

[13] M. Minnaert. The reciprocity principle in lunar photometry. *Astrophysical Journal*, 93:403–410, 1941.

[14] M. Oren and S.K. Nayar. Generalization of Lambert's reflectance model. In *SIGGRAPH 94 Conference Proceedings*, pages 239–246, Orlando, Florida, July 1994.

[15] B.T. Phong. Illumination for computer generated pictures. *Communications of the ACM*, 18(6):311–317, 1975.

[16] P. Poulin and A. Fournier. A model for anisotropic reflection. *Computer Graphics*, 24(4):273–282, August 1990.

[17] Ch. Schlick. A customizable reflectance model for everyday rendering. In *Proceedings of the Fourth Eurographics Workshop on Rendering*, pages 73–83, Paris, France, June 1993.

[18] Ch. Schlick. A survey of shading and reflectance models. *Computer Graphics Forum*, 13(2):121–131, June 1994.

[19] P. Schröder and W. Sweldens. Spherical wavelets: Efficiently representing functions on the sphere. In *SIGGRAPH 95 Conference Proceedings*, pages 161–172, Los Angeles, California, August 1995.

[20] P. Shirley and K. Chiu. Notes on adaptive quadrature on the hemisphere. Technical Report 411, Department of Computer Science, Indiana University, Bloomington, Indiana, 1994.

[21] K.E. Torrance and E.M. Sparrow. Off-specular peaks in the directional distribution of reflected thermal radiation. In *Transactions of the ASME*, pages 1–8, Chicago, Ill., November 1965.

[22] K.E. Torrance and E.M. Sparrow. Theory for off-specular reflection from roughened surfaces. *Journal of the Optical Society of America*, 57(9):1105–1114, September 1967.

[23] G.J. Ward. Measuring and modeling anisotropic reflection. *Computer Graphics*, 26(2):265–272, July 1992.

[24] S.H. Westin, J.R. Arvo, and K.E. Torrance. Predicting reflectance functions from complex surfaces. *Computer Graphics*, 26(2):255–264, July 1992.